Bedford, J., Moreno, M., Li, S., Oncken, O., Baez, J. C., Bevis, M., Heidbach, O., Lange, D. (2016): Separating rapid relocking, afterslip, and viscoelastic relaxation: An application of the postseismic straightening method to the Maule 2010 cGPS. - *Journal of Geophysical Research*, *121*, 10, pp. 7618—7638.

DOI: http://doi.org/10.1002/2016JB013093

AGU PUBLICATIONS

JGR

Journal of Geophysical Research: Solid Earth

RESEARCH ARTICLE
10.1002/2016JB013093

Key Points:
- The postseismic straightening method facilitates the parameterization of relocking, afterslip, and viscoelastic relaxation
- Plate interface relocking is the dominant process that causes the veering of cGPS displacements
- The isolated afterslip time function is in good agreement with the time function of cumulative aftershock number

Supporting Information:
- Supporting Information S1
- Movie S1
- Movie S2
- Table S1

Correspondence to:
J. Bedford,
jbed@gfz-potsdam.de

Citation:
Bedford, J., M. Moreno, S. Li, O. Oncken, J. C. Baez, M. Bevis, O. Heidbach, and D. Lange (2016), Separating rapid relocking, afterslip, and viscoelastic relaxation: An application of the postseismic straightening method to the Maule 2010 cGPS, *J. Geophys. Res. Solid Earth*, *121*, 7618–7638, doi:10.1002/2016JB013093.

Received 13 APR 2016
Accepted 9 OCT 2016
Accepted article online 12 OCT 2016
Published online 30 OCT 2016

Separating rapid relocking, afterslip, and viscoelastic relaxation: An application of the postseismic straightening method to the Maule 2010 cGPS

Jonathan Bedford[1], Marcos Moreno[1], Shaoyang Li[1], Onno Oncken[1], Juan Carlos Baez[2], Michael Bevis[3], Oliver Heidbach[1], and Dietrich Lange[4]

[1]Deutsches GeoForschungsZentrum, Potsdam, Germany, [2]Centro Sismológico Nacional, Universidad de Chile, Santiago, Chile, [3]Department of Geography, Ohio State University, Columbus, Ohio, USA, [4]GEOMAR Helmholtz Centre for Ocean Research, Kiel, Germany

Abstract The postseismic deformation captured with continuous Global Positioning System (cGPS) monitoring following many recent megathrust events has been shown to be a signal composed of two dominant processes: afterslip on the plate interface and viscoelastic relaxation of the continental and oceanic mantles in response to the coseismic stress perturbation. Following the south central Chile 2010 Maule M_w 8.8 earthquake, the time series from the regional cGPS network show a distinct curvature in the pathway of the horizontal motion that is not easily fit by a stationary decaying pattern of afterslip in combination with viscoelastic relaxation. Here we show that with realistic assumptions about the long-term decay of the afterslip signal, the postseismic signal can be decomposed into three first-order contributing processes: plate interface relocking, plate interface afterslip, and mantle viscoelastic relaxation. From our analyses we conclude that the plate interface recovers its interseismic locking state rapidly (model space ranges between an instant recovery and a period of 1 year), a finding that supports laboratory experimental evidence as well as some recent studies of aftershocks and postseismic surface deformation. Furthermore, relocking is the main cause of the curvature in the cGPS signal, and this study presents a plausible range of geodetic relocking rates following a megathrust earthquake.

1. Introduction

The continuous geodetic observation of subduction zones by means of the Global Navigation Satellite System (GNSS), widely referred to as cGPS monitoring [*Bock and Melgar*, 2016], provides us with data that are especially useful for constraining physical properties and mechanical behavior of the subduction plate interface. By using analytical functions describing surface motions due to dislocation in an elastic half-space [*Okada*, 1985], we can model the subduction zone plate interface kinematics according to the recorded surface displacements for all phases of the megathrust earthquake seismic cycle [e.g., *Simons et al.*, 2011]. These kinematic patterns, if correctly mapped, are crucial for estimating the remaining seismic potential (slip deficit) of a margin segment [*Moreno et al.*, 2012]. The estimation of afterslip—which is thought to release as much as 30% to >100% of the coseismic moment on the interface and is therefore an important consideration in the slip deficit calculation [e.g., *Heki et al.*, 1997; *Bürgmann et al.*, 2001; *Ozawa et al.*, 2004; *Perfettini et al.*, 2010]—is complicated by the presence of other postseismic processes in the signal, with the most commonly investigated simultaneous postseismic process being viscoelastic relaxation. In this study we are dealing with the near-field cGPS data for the first 4 years following the 2010 Maule M_w 8.8 earthquake of south central Chile with the aim of distinguishing the major contributing postseismic processes in the cGPS time series.

Figure 1 shows the selection of cGPS used in this study, with the stations covering distances of approximately 100–300 km from the trench. This station coverage is near enough to the trench to capture the plate interface kinematics and extends far enough to capture the mantle relaxation processes. The Maule earthquake broke a segment of the plate boundary between the Nazca and South American plates, and the rupture features of the main earthquake have been well documented, with most models in agreement [*Delouis et al.*, 2010; *Moreno et al.*, 2010; *Vigny et al.*, 2011; *Bedford et al.*, 2013]. Until now, the Maule postseismic data have been modeled with purely elastic assumptions to give a preliminary diagnosis of the afterslip pattern and spatiotemporal

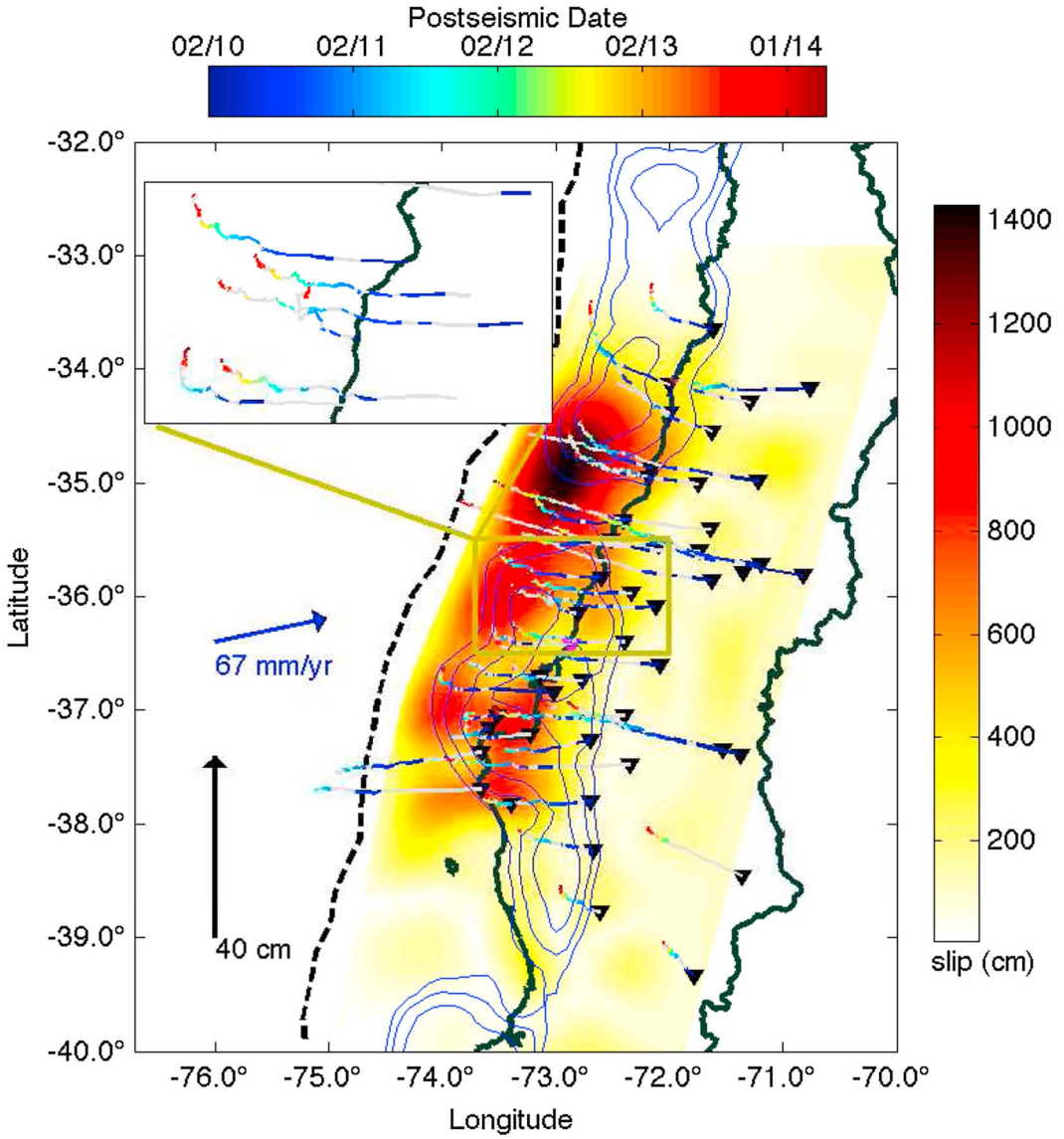

Figure 1. Plot of the study area. The black dashed line is the trench where the subducting Nazca plate meets the overriding South America plate. Thick black lines show the Chilean coastline and the border with Argentina. Blue contours show the interseismic locking model [*Moreno et al.*, 2011] with contour intervals at 0.7, 0.8, and 0.9 locking degree (1 and 0 would indicate a fully locked and fully decoupled plate interface, respectively). The colored distribution shows the coseismic slip distribution [*Bedford et al.*, 2013]. The black triangles indicate the location of the postseismic continuous GPS stations used in this study. Color scale shows the evolution of the horizontal pathway at each station. Curvature can clearly be seen at most stations. The inset shows a zoom in of postseismic horizontal deformation pathways for the region enclosed by the gold box.

characteristics [*Bedford et al.*, 2013; *Vigny et al.*, 2011]. However, questions remain as to the validity of such purely elastic models when the viscoelastic response is neglected. Comparisons of afterslip, coseismic slip, and aftershocks have yielded promising spatial relations that suggest a predominance of afterslip contributing to the captured near-field cGPS [*Bedford et al.*, 2013], especially since there is a clear linear relation between the local number of plate interface aftershocks and local cGPS motion and that the locations of modeled afterslip and the majority of aftershocks are in good agreement [*Lange et al.*, 2014].

This study uses postseismic horizontal motions (Figure 1) that have been captured over the first 4 years following the earthquake. At many stations the postseismic signal in space is curved, with the curvature occurring in a clockwise direction. Curvature in the anticlockwise sense is not observed. Postseismic processes that could be combining to produce this spatial curvature in time include (1) megathrust plate interface afterslip,

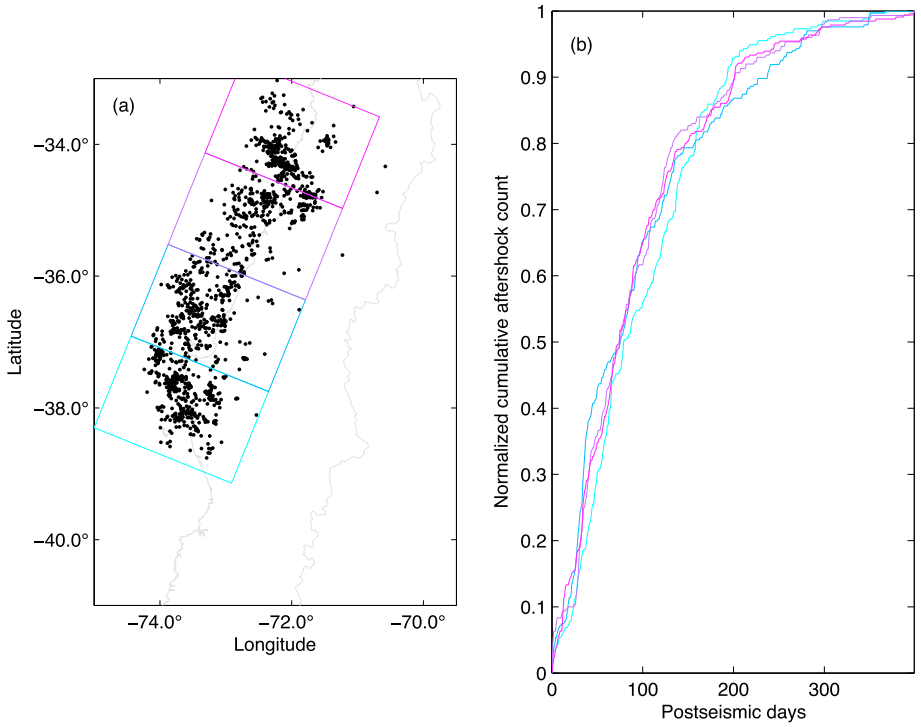

Figure 2. (a) Maule plate interface aftershocks are shown in black [*Hayes et al.*, 2013]. The coastline and political borders are shown in grey. The zones for the along-strike analysis of cumulative aftershock number are the boxes, with the colors corresponding to the lines plotted in Figure 2b. Aftershocks greater than 10 km from the plate interface geometry model [*Tassara and Echaurren*, 2012] have been discarded in this analysis. (b) The normalized cumulative aftershock count for the zones of Figure 2a.

(2) viscoelastic relaxation of the mantle, and (3) the relocking of the megathrust plate interface. The aim of this study is to investigate the relative contributions of these candidate postseismic processes to the signal. We use simple models to represent each process while assuming that the curvature in the signal results from a combination of a spatially linear afterslip signal with one of (a) viscoelastic relaxation, (b) relocking, or (c) both viscoelastic relaxation and relocking.

2. Methods

2.1. Isolating Afterslip Signal With a Straightness Assumption

Curvature in the spatial pathway of the postseismic cGPS motions is due to either a single postseismic process that produces curved motions or a combination of processes with different decay rates and azimuthal tendencies. While slip on the subduction plate interface has on occasions been shown to produce spatially curved predictions in time [e.g., *Radiguet et al.*, 2011], this curvature has been attributed to a migration of slip. For spatiotemporal models of afterslip on the plate interface following great subduction earthquakes, slip migration has not been apparent [*Bedford et al.*, 2013; *Shirzaei et al.*, 2014], and these models exhibit a predominantly spatially stationary afterslip pattern that decays in magnitude with time. Cumulative afterslip on the plate interface has been shown to be linearly related to the cumulative number of aftershocks [e.g., *Perfettini and Avouac*, 2007; *Lange et al.*, 2014] meaning that an independent indicator of the extent of afterslip migration is the difference between normalized cumulative aftershock decays at various locations along strike of the rupture: Figure 2 shows the normalized cumulative aftershock time functions along strike of the Maule rupture zone for the seismic catalogue of *Hayes et al.* [2013]. Here we see that the normalized decay in number of aftershocks along strike with time is very similar. If the aftershocks and afterslip are temporally related as suggested by *Perfettini and Avouac* [2007] and *Lange et al.* [2014], then the ratio between slip magnitudes at any two locations is likely to be constant with time, giving a nonmigrating afterslip pattern.

Proceeding with the assumptions that the afterslip pattern following the Maule megathrust is spatially stationary and decaying in magnitude, with relative magnitudes of afterslip at any two locations constant through

time, we can attempt to isolate the afterslip signal based on the expected afterslip signal characteristics. An afterslip model with these assumptions would produce the following characteristic features in the cGPS signal: (1) a spatially linear, nonveering, motion as a function of time and (2) identical normalized time functions of cumulative motions at all prediction locations on the surface.

The characteristic of *spatial straightness* (spatial linearity) in the afterslip surface signal is explained by considering the individual components of the cGPS signal. For simplicity, we will consider the horizontal components (east and north), although this explanation would hold for a consideration all three components of the signal. The individual east and north afterslip signals are

$$E(t) = C_E \log(1 + \delta t/T) \tag{1}$$

$$N(t) = C_N \log(1 + \delta t/T) \tag{2}$$

where C_E and C_N are impulse responses from the elastic dislocation Green's functions [*Okada*, 1985] relating the particular afterslip pattern to the surface motion, and the logarithmic term is a typical function used in long-term plate trajectory models [e.g., *Bevis and Brown*, 2014] that characterizes the postseismic decay with the time increment, δt, and time constant, T. Azimuth of the horizontal motion as a function of time can be found by taking the arc-tangent of equation (1) divided by (2), giving

$$\phi_{\text{afterslip}} = \arctan\left(C_E/C_N\right) \tag{3}$$

where $\phi_{\text{afterslip}}$ is the azimuth of surface motion due to afterslip with the discussed assumptions. Afterslip azimuth is clearly independent of time and therefore produces straight motion in the cGPS, without any veering. From equations (1) and (2) it follows that the cumulative horizontal motion as a function of time is

$$H(t) = \left(\sqrt{C_E^2 + C_N^2}\right) \log(1 + \delta t/T) \tag{4}$$

Given that the logarithmic term is dependent on the decay of the afterslip pattern, and that C_E and C_N are the impulse response of the stations from the calculations of the Green's functions for that particular afterslip pattern, then we can rewrite equation (4) as

$$H_i(t) = X_i \log(1 + \delta t/T) \tag{5}$$

where X_i is a constant multiplier unique to each station. If we normalize $H_i(t)$ for each station by dividing by the final horizontal cumulative displacement, the X_i term at each time step is canceled out and we are left with the normalized logarithmic time function at each station — the same normalized time function at each station (see Figure 3). Note that the time function of afterslip decay does not have to take the logarithmic form as written in the above equations: the straightness and identical normalized time functions of the surface signal would also be valid with a linear or power law decay of the afterslip signal.

With our assumptions of afterslip behavior and the characteristics of the consequential surface signal, we can isolate the afterslip signal by removing simultaneous postseismic processes that cause the horizontal motion to deviate (veer) from a straight course. Figure 4 shows schematically the combination of simultaneous postseismic processes (afterslip, relocking, and viscoelastic relaxation) in producing the measured cGPS signal.

By subtracting viscoelastic relaxation and relocking signals from the measured total signal, we leave behind the afterslip signal. On this premise we construct a parameter search method to explore the parameter space describing relocking rate and mantle viscosities below the elastic limits of the oceanic and continental plates. The best fitting parameters of relocking and viscoelastic relaxation produce a signal, which when subtracted from the data leaves behind a straight horizontal motion in the cGPS and similar normalized time functions. The first stage of the parameter search is to *straighten* the data by subtracting the viscoelastic relaxation and/or relocking predictions (see sections 2.4 and 2.3 for details of the prediction methods and ranges in these parameter spaces). For each combination of relocking and/or viscoelastic relaxation parameters we subtract

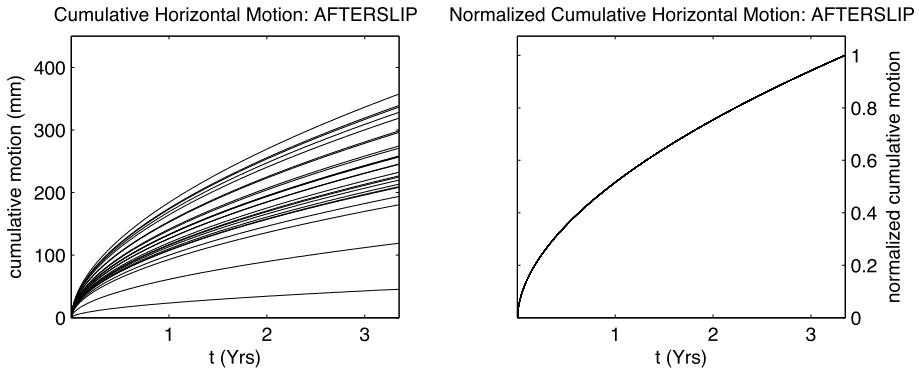

Figure 3. (left) The cumulative horizontal displacements as a function of time at a cGPS network. Displacements are predicted from a stationary afterslip pattern that decays at the same relative rate along the whole dimensions of the slipping zone. (right) The normalized horizontal displacement time functions of Figure 3 (left). Here we demonstrate that all cumulative horizontal displacement histories collapse to the same normalized time function if they are coming from a stationary pattern of decaying slip, where the relative magnitudes of adjacent slip patches are constant.

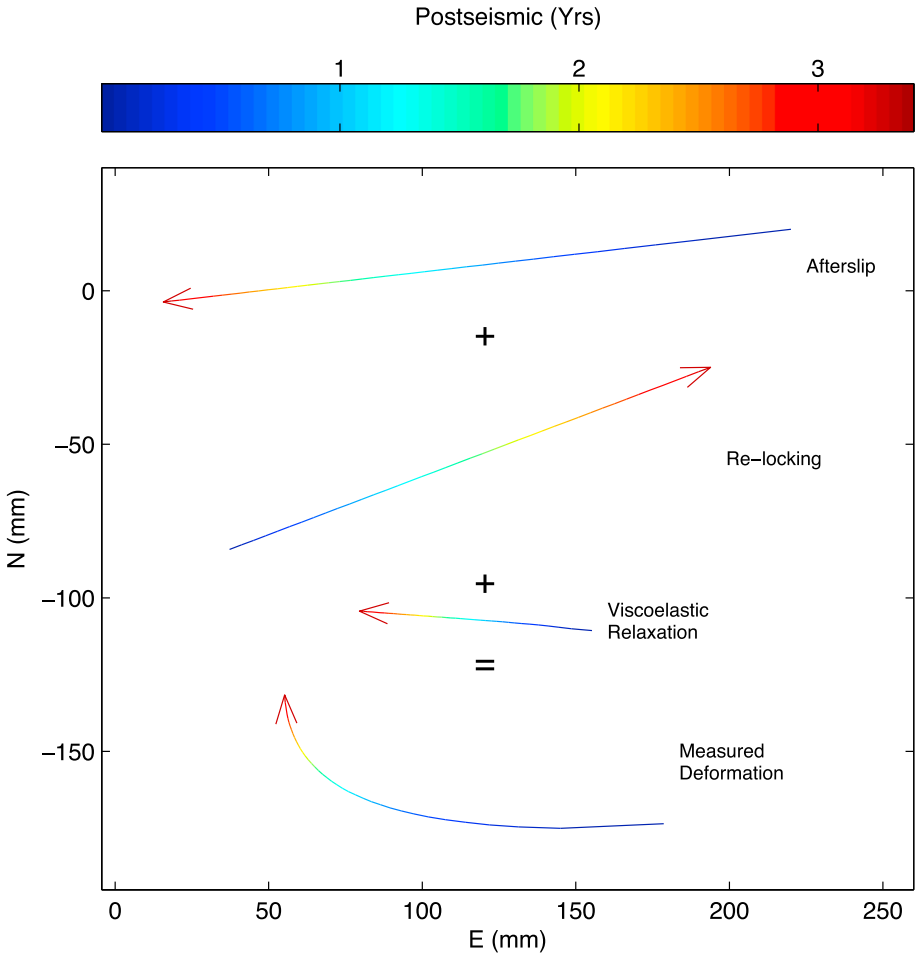

Figure 4. A schematic example of the simultaneous surface signals of afterslip, relocking, and viscoelastic relaxation which contribute to the measured signal in east-north space. Colors correspond to the elapsed time (shown in the color bar at the top of the figure).

the predicted signals from the data (equations (6) and (7)) and fit a linear trend to the remaining signal with a least squares minimization of equation (8) to find the gradient, m:

$$A_E^i(t) = D_E^i(t) -_p V_E^i(t) -_p B_E^i(t) \tag{6}$$

$$A_N^i(t) = D_N^i(t) -_p V_N^i(t) -_p B_N^i(t) \tag{7}$$

$$A_E^i(t)m = A_N^i(t) \tag{8}$$

where $D_E^i(t)$, $D_N^i(t)$, $A_E^i(t)$, $A_N^i(t)$, ${}_pV_E^i(t)$, ${}_pV_N^i(t)$, ${}_pB_E^i(t)$, and ${}_pB_N^i(t)$ are the east and north components of displacement as a function of time for the measured signal (*D*ata), assumed remaining *A*fterslip, predicted *V*iscoelastic relaxation, and predicted *B*ackslip (relocking) for each station, i. By multiplying the east component of the remaining signal, $A_E^i(t)$, by the gradient, m, we can create predictions for the north motion, ${}_pA_N^i(t)$ (equation (9)) and we can evaluate the fit of the predicted north motion to the actual north motion at all stations, i, by taking the sum of the squared residuals (equation (10)):

$${}_pA_N^i(t) = mA_E^i(t) \tag{9}$$

$$S = \sum_{n=1}^{i} \sum_{t=f_i}^{l_i} \sqrt{\left(A_{tN}^i -_p A_{tN}^i\right)^2} \tag{10}$$

where for each station, i, the start and end times f_i and l_i are determined by data availability (gaps in the data between available epochs are not considered in the summation). A straightness misfit S is thus calculated for each combination of model parameters.

Following the straightening, the remaining signals that are assumed to be afterslip ($A_E^i(t)$ and $A_N^i(t)$) are fed into an inversion for cumulative afterslip (see section 2.4 for details on inversion). For this step we must have data available for as many stations as possible and for as long an epoch as possible. We choose, therefore, the epoch between 4 April 2010 and 7 August 2013 and take the cumulative displacements from the $A_E^i(t)$ and $A_N^i(t)$ signals as the static displacements for the afterslip inversion. Inverting the cumulative afterslip signals produces a set of cumulative afterslip predictions. To create a time series of afterslip predictions (${}_pA_E^i(t)$ and ${}_pA_N^i(t)$), we multiply the cumulative predictions by the mean of the normalized cumulative horizontal displacement of the isolated afterslip signals (e.g., Figure 3). This multiplication assumes that the cumulative isolated afterslip signals can be fit well by an afterslip model and that the isolated afterslip signals have very similar time functions. Isolated afterslip signals that do not adhere to these assumptions result in a poor fit to the time series upon combination of the predicted afterslip signals with the viscoelastic relaxation and relocking time series predictions:

$$\chi_m^2 = \sum_{n=1}^{i} \sum_{t=f}^{l} \sqrt{\left(D_{tE}^i -_p A_{tE}^i -_p B_{tE}^i -_p V_{tE}^i\right)^2 + \left(D_{tN}^i -_p A_{tN}^i -_p B_{tN}^i -_p V_{tN}^i\right)^2} \tag{11}$$

where χ_m^2 is the measure of misfit for the whole data set for each of the m model parameter combinations of the parameter search, and f and l are the first and last days of the time series between the epoch considered for the inversion of the afterslip model.

The results of the parameter search are separated into three ensembles (see section 3): (1) Afterslip + Viscoelastic Relaxation + Relocking (AS + RL + VR / RL + VR straightening), (2) Afterslip + Viscoelastic Relaxation (AS + VR / VR-only straightening), and (3) Afterslip + Relocking (AS + RL / RL-only straightening).

2.2. Data Processing

Following the Maule earthquake, a dense network of 67 cGPS stations was deployed and maintained in a multinational effort [e.g., *Vigny et al.*, 2011]. In this study we use 44 stations for which to perform the data straightening and 25 stations for the afterslip inversion and final time series misfits evaluation. The unfortunate discarding of some stations before inversion for afterslip is due to the requirement that the data used to model afterslip have a common start and end time, and that the epoch between these times is as large as possible. Data for all stations were organized in 24 h periods. Each observation was processed using the

Table 1. Reference Stations Used in the Processing of the Maule Postseismic Time Series

Station Name	Latitude (deg)	Longitude (deg)
SANT	−33.150	−70.669
AREQ	−16.466	−71.493
LPGS	−34.907	−57.932
UNSA	−24.728	−65.408
IQQE	−20.274	−70.132
COPO	−27.385	−70.338
COYQ	−45.514	−71.892
PARC	−53.137	−70.880
RIO2	−53.786	−67.751
FALK	−51.694	−57.874
VBCA	−38.701	−62.269
CHPI	−22.687	−44.985
BRAZ	−15.948	−47.878
UFPR	−25.448	−49.231
ISPA	−27.125	−109.3444

Bernese GPS Software 5.2 [*Dach et al.*, 2007]. Precise orbit and earth rotation parameters were used from International GNSS Service final products [*Dow et al.*, 2009]. During the processing, the antenna phase center was reduced using absolute calibration, and double differences were modeled in L3, using elevation masks of 10 and a sampling rate of 30 s. To form the single differences, a phase strategy of maximum observations was used. No a priori troposphere model was applied. The troposphere parameters were estimated in all steps of parameter estimation. Corrections of the troposphere zenith delay for each station were estimated every 2 h. We used a Vienna Mapping Function [*Boehm et al.*, 2006] to compute the correction. The elevation-dependent weighting was applied using the function $\cos(z)^2$. We stacked the free solutions in a normal equation file for each day. For the datum definition we used the minimum constraint approach, applying the No Net Rotation (NNR) and No Net Translation (NNT) conditions for a group of selected reference stations (see Table 1). Coordinates for each reference station were obtained from the global polyhedron weekly solution [*Dow et al.*, 2009]. Our results are compatible with ITRF2008 [*Altamimi et al.*, 2011]. The horizontal cGPS data are corrected for sudden displacements attributed to large aftershocks by means of a step detection algorithm based on a canny filter. Steps were removed by subtraction of the displacement between the consecutive points of the confirmed sudden displacement. The remaining signals contain a strong seasonal periodicity in the north component: We decided against filtering away this signal, rather opting to avoid the trade-off between removal of the seasonal signal and preservation of the long-term decay signal, the long-term decay signal being crucial for parameterizing the postseismic processes.

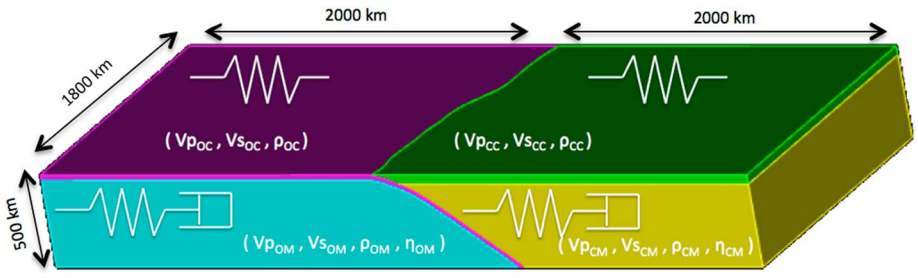

Figure 5. The geometry and division of materials for the finite element method (FEM) modeling of postseismic viscoelastic response. We consider an elastic oceanic slab with elastic thicknesses of 30 km (purple) and an elastic continental upper lithosphere with an elastic thickness of 50 km (green). Below the elastic oceanic and continental units we have isotropic linear Maxwell viscoelastic mantle units (referred to in this study as continental and oceanic mantles). In each forward model of postseismic viscoelastic response, we assign a different combination of viscosities to the two mantles. List of fixed elastic parameters can be found in Table 2.

Table 2. Elastic Parameters Used in the FEM Simulation

Material Block	Shear Modulus (GPa)	Poisson's Ratio
Continental upper lithosphere	40	0.27
Oceanic slab	46	0.3
Continental mantle	78	0.25
Oceanic mantle	78	0.25

2.3. Modeling Viscoelastic Relaxation

Modeling of surface motions due to viscoelastic relaxation is conducted using the finite element method (FEM). The model neglects the curvature of the Earth's surface and consists of four material blocks: the downgoing elastic oceanic slab, the viscoelastic oceanic asthenospheric mantle, the elastic continental upper lithosphere, and the viscoelastic continental mantle (Figure 5). For simplicity, we hereafter refer to the assumed viscoelastic portions of the mantle as the mantle.

In our model, the elastic continental upper lithosphere extends to a uniform depth of 50 km, and the subducting slab has a thickness of 30 km. Both the subducting slab and overriding continental upper lithosphere are assumed to be purely elastic bodies (see Table 2 for list of elastic parameters), whereas the two mantles are assigned linear Maxwell viscoelastic behavior with the elastic parameters constrained from gravity and tomography studies [*Hicks et al.*, 2012; *Tassara and Echaurren*, 2012]. The plate interface is defined by the gravity and seismicity studies [*Tassara and Echaurren*, 2012], and the mesh extends approximately 2000 km both east and west from the trench, and the along-strike length of the mesh is 1800 km. The depth of the mesh is 500 km; therefore, there is ample distance in all directions from the coseismic rupture zone to the bounds of the mesh to avoid boundary artifacts. We employed controlled meshing to mesh the tetrahedral elements more finely at the zone of interest in the vicinity of the rupture, and the mesh size expands toward the volume boundary to save on computational expense. The mesh consists of over 1.2×10^6 elements. The bottom of the mesh is free to slide laterally on its plane, as are the east and west boundaries. The north and south boundaries are unconstrained. FEM simulation is run using the open source solver PyLith [*Aagaard et al.*, 2013]. The coseismic rupture distribution and magnitude are taken from *Bedford et al.* [2013]. Combinations of oceanic and continental mantle viscosities are varied for each simulation between 1×10^{19} and 1×10^{20} Pa s for the continental mantle and between 1×10^{19} and 2.5×10^{20} Pa s for the oceanic mantle in accordance with the ranges of linear Maxwell viscosities found by other relevant studies of both subduction zones [*Li et al.*, 2015; *Diao et al.*, 2014; *Hu et al.*, 2004] and general upper mantle values [*Bürgmann and Dresen*, 2008; *Mitrovica*, 1996].

Figure S1 in the supporting information shows an example of the predicted time evolution of surface motions due to different combinations of oceanic and continental mantle viscosities. The veering of the horizontal motion can be in both a clockwise and an anticlockwise sense for the isolated viscoelastic relaxation signal.

The simplicity in the geometry and rheology of the model was chosen to preserve the computational cost of the study. If we were to investigate the effects at full range of proposed rheologies [e.g., Burgers *Wang et al.*, 2012, or Power Law *Freed et al.*, 2006], we would need to investigate at least double the amount of parameters in the viscoelastic units. Similarly, if we were to test the layering in viscosity, by, for example, introducing separate lithospheric and asthenospheric mantles, or a vertical gradient in viscosity, we would introduce further parameters to our search that would make the study too computationally expensive as well as make the results much more difficult to interpret.

2.4. Modeling Relocking

Surface motions due to plate interface relocking are forward modeled using the backslip assumption [*Savage*, 1983], whereby the surface motions due to locking on the plate interface can be modeled from dislocations on the plate interface in the direction of plate convergence [see *Kanda and Simons*, 2010, Figure 1]. Most of our input time functions correspond to the power law equation

$$L(t) = at^b \tag{12}$$

where L is the fraction of original locking degree as a function of time, t (in days), and a and b are variables of the time function. Other time functions take a flat rate of the form:

$$L(t) = c \tag{13}$$

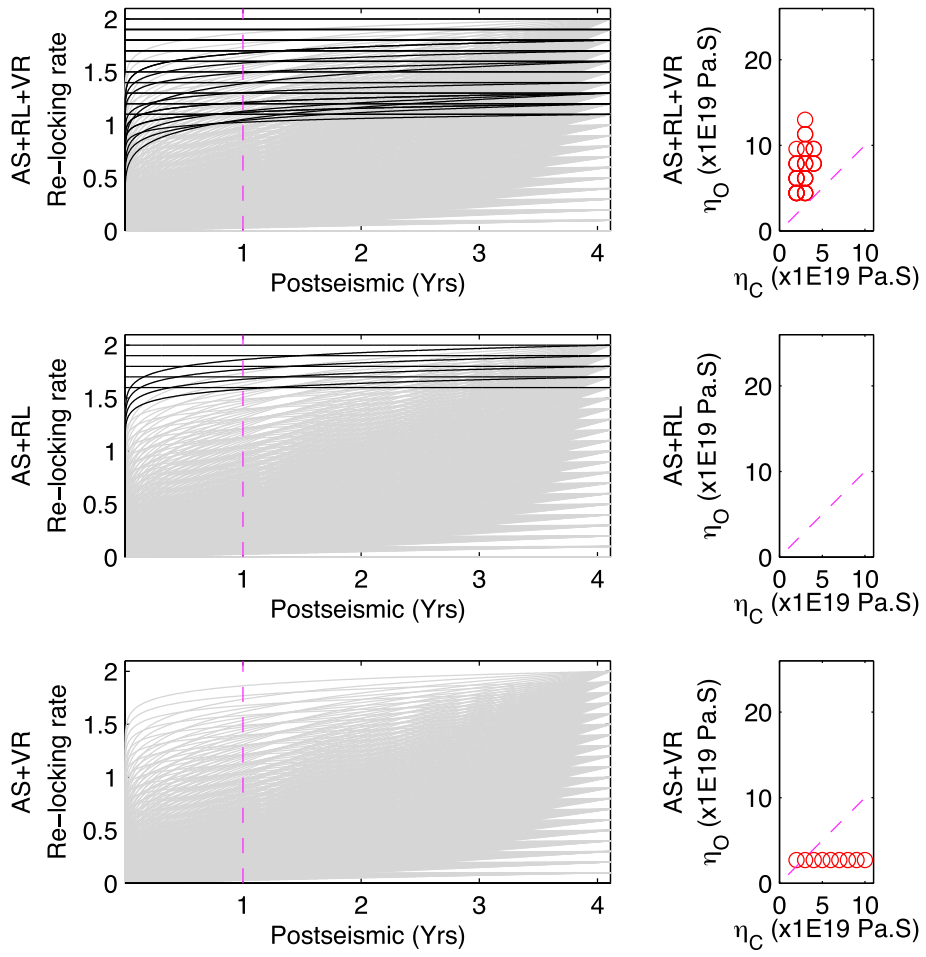

Figure 6. (left column) Relocking rates: In grey are all the relocking rates in the parameter space, and in black are the best performing relocking rates of the parameter search. (right column) The best performing combinations of oceanic and continental linear Maxwell viscosities. (top row) The combined afterslip, relocking, and viscoelastic relaxation model (AS + RL + VR) and the top 44 parameter combinations. (middle row) The afterslip and relocking model (AS + RL) and the top 10 parameter combinations. (bottom row) The afterslip and viscoelastic relaxation model (AS + VR) and the top 9 parameter combinations. Most relocking rates indicate a return to interseismic locking degree or higher within 1 year following the earthquake. Note that the top model parameter combinations in each case are defined in the misfit spaces for both the recombined time series and the afterslip inversions (see Figure S4).

where c is the assumed fraction of locking degree and the locking degree is independent of time. All time functions are listed in Table S1 in the supporting information.

For each time function of relocking, L(t), we produce a suite of horizontal surface predictions at the cGPS locations by multiplying the time function with the locking map of *Moreno et al.* [2011] (see Figure 1) and the interseismic incoming plate convergence velocity of 67 mm/yr [*Sella et al.*, 2002] to predict the evolution of displacements from Green's functions relating surface motion due to dislocations in an elastic half-space. The calculation of Green's functions assumed elastic parameters of 0.25 for Poissons ratio and 35 GPa for shear modulus. These parameters were derived using average values of forearc Vs and density, using seismic tomography and gravity studies of the region [*Hicks et al.*, 2012; *Tassara and Echaurren*, 2012]. Relocking direction was assumed to be in line with the azimuth of plate convergence [*Sella et al.*, 2002], and the plate interface was represented with the same geometry as that used in the construction of the finite element modeling. The horizontal surface displacements predicted by the relocking models consist of NE pointing landward signals that are spatially straight, since the ratio of magnitudes in the relocking pattern is constant in time for all time functions (e.g., equations (1)–(3)). The maximum locking rate allowed in the relocking time functions is set as 2 times the interseismic rate which allows for superinterseismic relocking in case of an increase in subduction velocity during the early postseismic—a phenomenon postulated by *Heki and Mitsui* [2013].

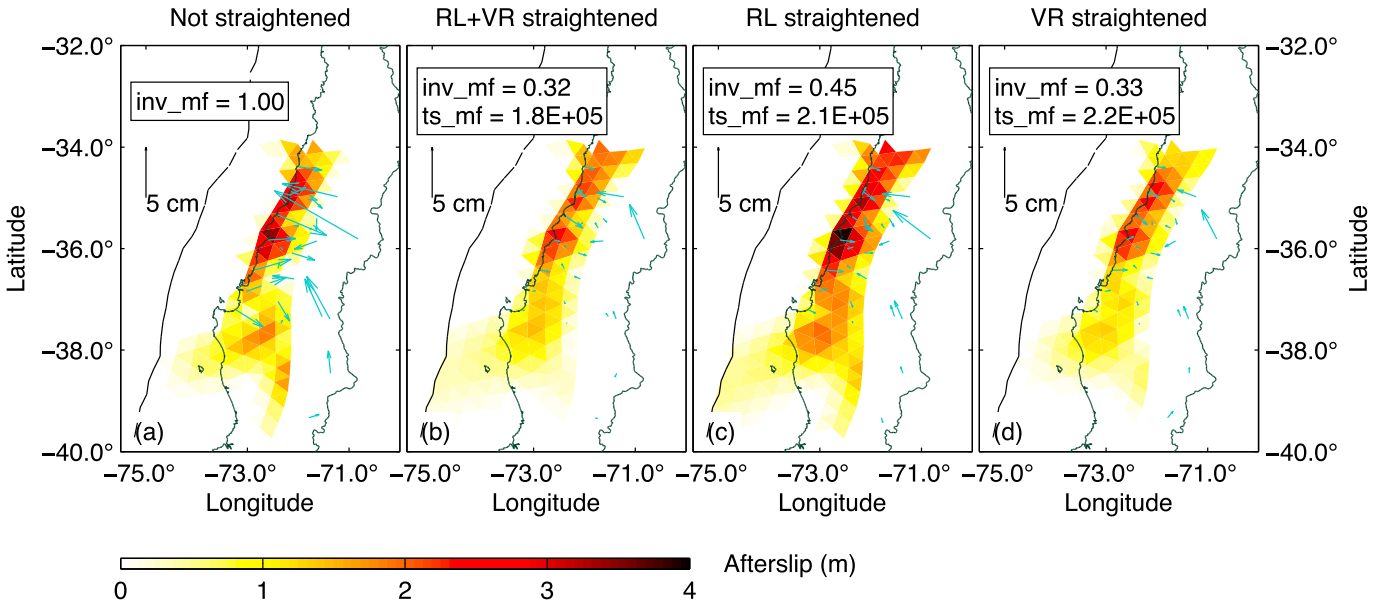

Figure 7. (a–d) The misfit vectors (data minus predictions) following the inversion for afterslip on the plate interface (blue vectors) and the afterslip distribution on the plate interface (color scale indicates the slip amount). The title of each panel shows the straightening method applied to the data before inversion. The relocking and viscosity parameters for each ensemble are chosen from the best fitting time series after inversion for afterslip on the plate interface. Inversion misfit (inv_misf) and misfit of the time series after recombination of afterslip with the other processes in the model ensemble (ts_misf) are shown in the inset boxes. The inversion misfit is normalized by the misfit of the nonstraightened data. The afterslip model from the cumulative displacement is greatly improved after corrections of additional processes (relocking and/or viscoelastic relaxation), particularly in the back arc. The inversion misfits for the RL + VR and VR-only straightening are very similar, whereas the RL-only straightening results in a slightly larger misfit in the back-arc stations. All straightening ensembles result in a poor fit to the easternmost station. The models that neglect viscoelasticity (i.e., Figures 7a and 7c) tend to have a deeper, higher-magnitude afterslip.

2.5. Modeling Afterslip

The afterslip models are obtained by inversion of surface motion for slip on the plate interface. The plate interface geometry used for the inversion is the same as the one used for the previous modeling steps. The forward problem is set out by the following equation:

$$GX = A \tag{14}$$

where G is the matrix of Greens functions relating unit motions on the plate interface to the elastically predicted surface motions at the cGPS stations, X is the vector containing slip magnitude at each patch, and A is the vector containing the surface displacements that we are inverting (the assumed isolated afterslip cumulative displacements). We apply a Laplacian smoothing constraint on the slip distribution [e.g., *Bedford et al.*, 2013], and for consistency this smoothing constraint is kept constant for the inversion of both the curved and straightened data. The azimuth of the horizontal component of the slip vector is constrained to be within 240° to 300° to avoid solutions with spurious slip directions. The Laplacian weighting factor is chosen by means of a subjective trade-off selection between model roughness [*Menke*, 1989] and misfit of the predicted displacements. The patches of the fault model extend to a maximum depth of 70 km. Displacements used in the inversion are the cumulative time series displacements between 4 April 2010 and 7 August 2013. This time period was chosen to maximize the number of stations with cumulative displacement coverage. Afterslip models for all favored parameter combinations of the three model ensembles are discussed in section 3.4.

3. Results

3.1. Straightening of Horizontal Motion

Figure S2 shows the result of the straightness misfit of the signals following the subtraction of the predicted viscoelastic relaxation and/or relocking signal from the data plotted as normalized straightness misfits.

We normalize the straightening misfit of the corrected signals by dividing by the straightening misfit of the uncorrected signals. The RL-only correction results in the straightest signals, with the best normalized straightness misfit being approximately 0.43. Over 100 of the 400 input time functions of relocking in the RL-only

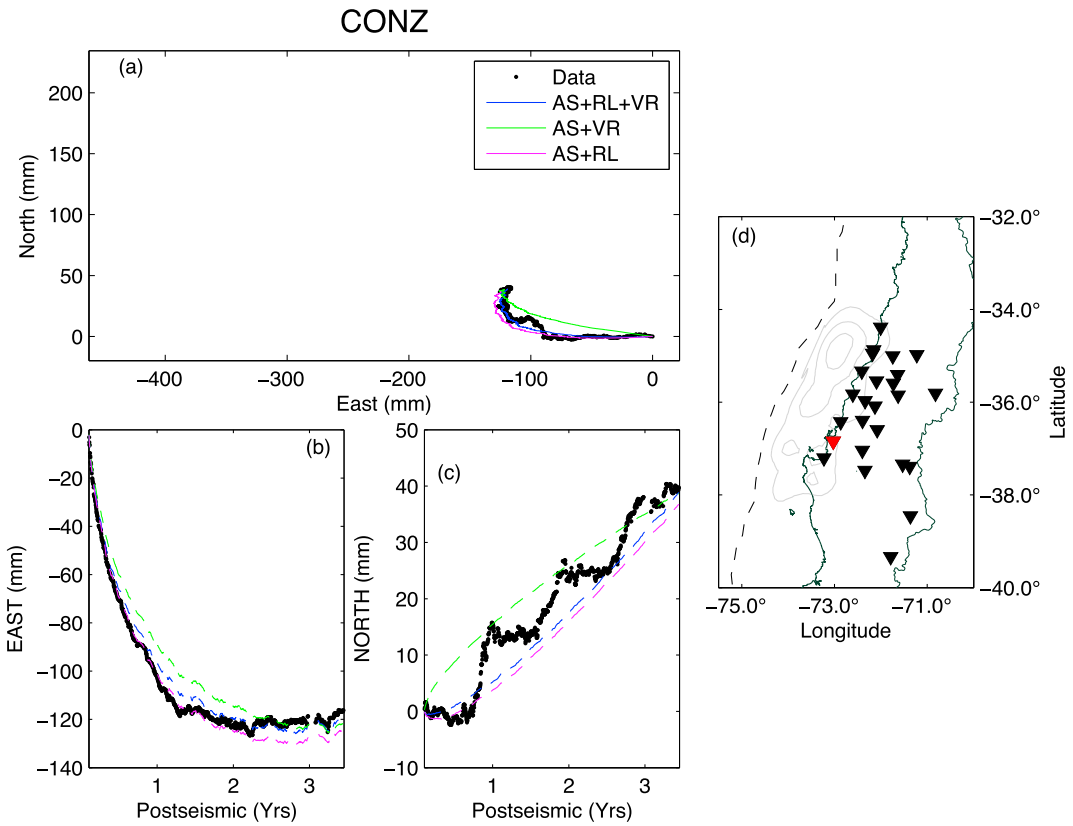

Figure 8. (a) The horizontal displacement pathway of the data and the predictions from the model ensembles (colors denoted in the legend). (d) The location of the station (red triangle) in the cGPS network (black triangles) and with respect to the coseismic slip distribution (grey contours). (b, c) The east and north displacements as a function of time for the data and predictions.

straightening result in a similar success in straightening. For the RL + VR straightening, the best straightened signal has a misfit of 0.48. This model ensemble has up to 10,000 out of 60,000 parameter combinations that straighten the signal to a similar success. The worst performing ensemble for straightening the signal is by VR-only, which has a normalized straightening misfit of 0.69. If we assume that the assumptions of the straightness for the afterslip model are valid (section 2.1) and that the assumption of viscoelastic rheology is not too oversimplified, then from Figure S2 it can be stated that the relocking is the dominant process causing the curvature in the time series. The nonuniqueness of the straightening performance in each ensemble type strongly depends on the sampling interval of the parameter space; i.e., there are many more locking time functions (600) than viscoelastic relaxation models (150) and therefore the nonuniqueness of the solution space could be decreased considerably by discarding many of the similar locking time functions.

3.2. Time Series Misfits Following Afterslip Inversion

Figure S3 shows the result of the time series fits following the inversion for afterslip and the recombination of the predicted afterslip time series with the relocking and/or viscoelastic relaxation signals. We can clearly see that the ensemble of three processes (AS + RL + VR) produces the best fits to the time series data (see section 3.5 for more details and examples of the time series). The time series misfit decreases by 22% when the relocking process is considered in addition to the afterslip and viscoelastic relaxation. Interestingly, the neglecting of a viscoelastic response, with just a model of relocking and afterslip (AS + RL), can fit the data slightly better than a model with just afterslip and viscoelastic response There exists some nonuniqueness in the solutions for all ensemble types (see section 3.3), although this nonuniqueness is not as pronounced as for the straightening results. This is because there are some combinations of parameters that will straighten the horizontal motions very well, yet the remaining signals will have too much of a variation in their normalized time functions and/or the remaining signals will not be fit so well with a least squares minimization of the afterslip on the plate interface.

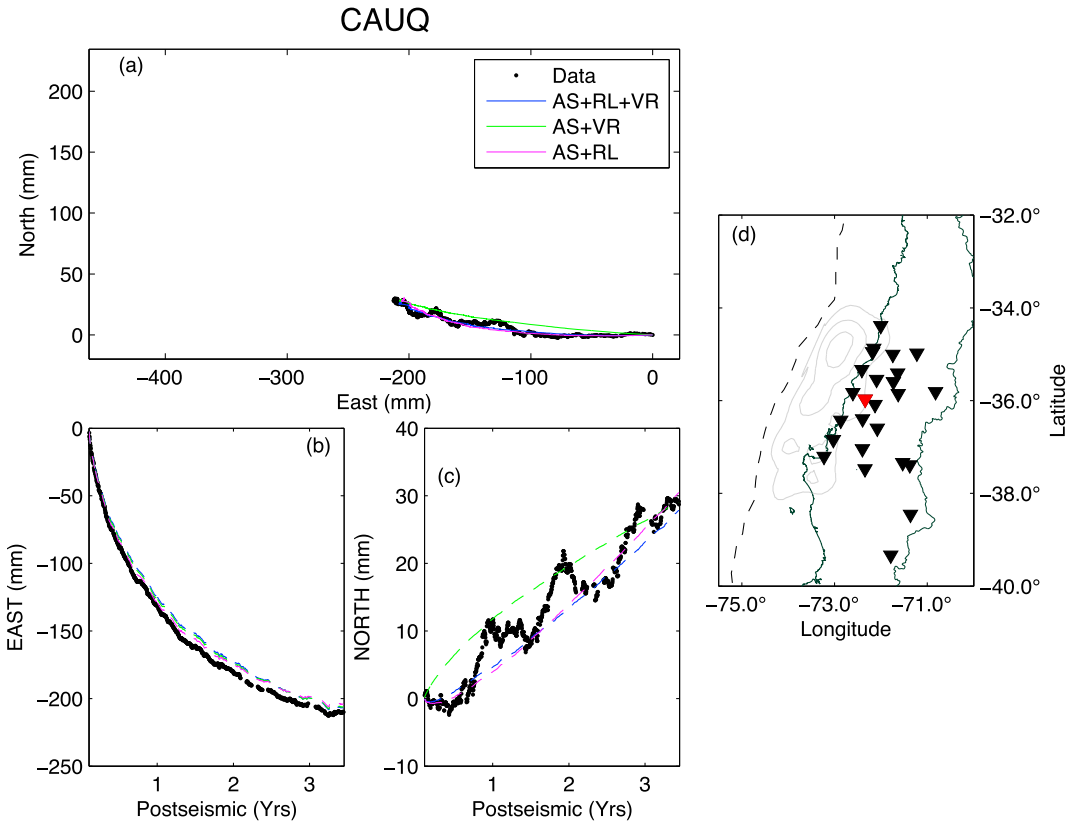

Figure 9. (a) The horizontal displacement pathway of the data and the predictions from the model ensembles (colors denoted in the legend). (d) The location of the station (red triangle) in the cGPS network (black triangles) and with respect to the coseismic slip distribution (grey contours). (b, c) The east and north displacements as a function of time for the data and predictions.

3.3. Best Fitting Parameters

Figure 6 shows the best fitting time functions and viscosity combinations for each ensemble of the parameter search with Figure S4 showing the misfit space for both the afterslip inversion and recombined time series within which these best fitting models are defined.

We can see that the best (AS + RL + VR) models have locking time functions that indicate a recovery of interseismic locking rate within 1 year. Also, in the locking time function solution space for this ensemble are superinterseismic locking rates. The parameter space of the parameter search includes superinterseismic rates since this has been postulated by *Heki and Mitsui* [2013] based on the postseismic velocity change of locked segments adjacent to ruptured segments. The nonuniqueness of the solution means that we cannot distinguish between flat rates and power law time functions of locking. For the three-process ensemble, the range of relocking time functions suggests that the interseismic locking rate, if not recovered almost instantaneously, is recovered within a year. The AS + RL ensemble requires a superinterseismic locking rate that is effective immediately (or almost immediately) in the postseismic phase. The best fitting viscosity combinations of the oceanic and continental mantles for the three-process (AS + RL + VR) model indicate a more viscous oceanic mantle than continental mantle. The oceanic mantle viscosity is between the ranges of 4×10^{19} and 1.1×10^{20} Pa s, and the continental mantle viscosity is between the ranges of 2×10^{19} and 4×10^{19} Pa s; therefore, the fitting of the time series with the three-process model is more sensitive to the continental mantle rather than the oceanic mantle viscosity, so long as the oceanic mantle viscosity is greater than 4×10^{19} Pa s. The range of locking time functions that produce the best time series fits in the two-process model of afterslip and relocking (AS + RL) is similar to the solution space of the three-process model. The difference being locking rates of the AS + RL model after 1 year of postseismic time tends to be greater than 1.4 the interseismic rate, compared to 1.1 for the three-process model. For the model ensemble of viscoelastic relaxation and afterslip (VR + AS) the oceanic mantle viscosity tends to be less than the continental mantle viscosity. The oceanic mantle

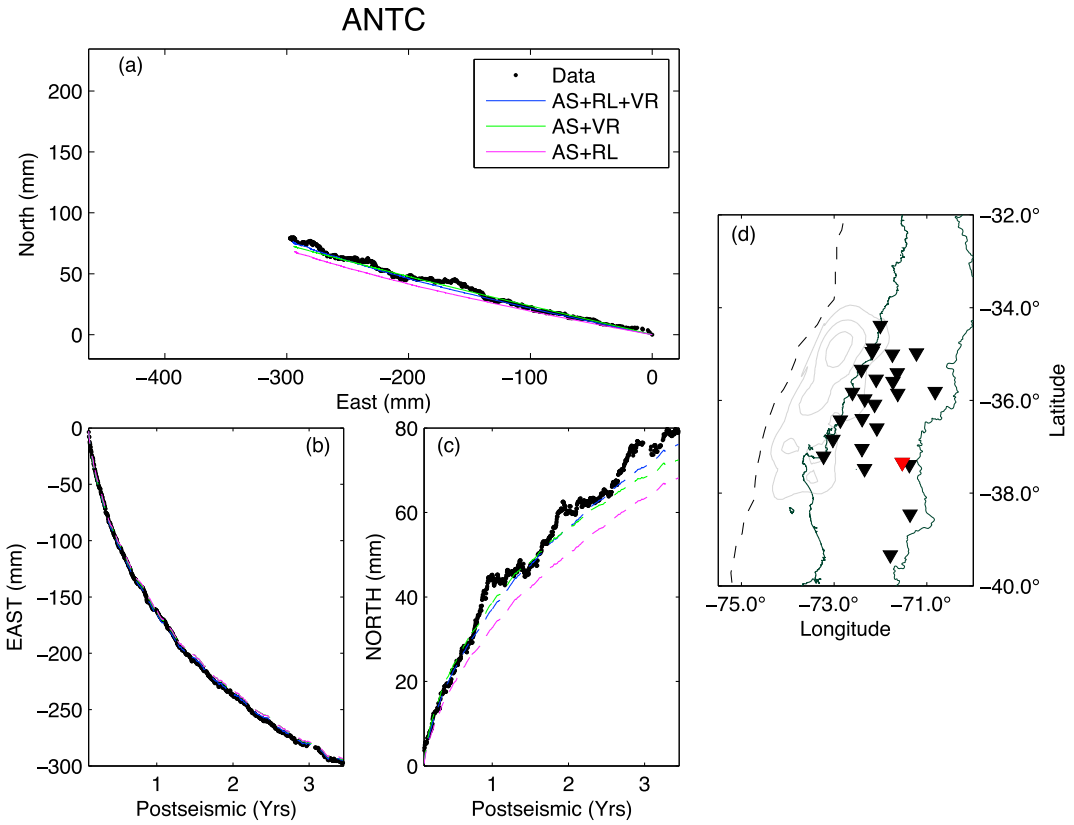

Figure 10. (a) The horizontal displacement pathway of the data and the predictions from the model ensembles (colors denoted in the legend). (d) The location of the station (red triangle) in the cGPS network (black triangles) and with respect to the coseismic slip distribution (grey contours). (b, c) The east and north displacements as a function of time for the data and predictions.

viscosity is 3×10^{19} Pa s, and the continental mantle viscosity is between the ranges of 2×10^{19} and 1×10^{20} Pa s; therefore, the fits of this model ensemble are more sensitive to the viscosity of the oceanic, rather than the continental, mantle.

3.4. Comparing Afterslip Models

As explained in section 2.1, the predicted afterslip signals are obtained by inverting the cumulative displacements before recombining with the mean of the normalized time functions of the time series between the start and the end of the epoch of cumulative displacement. A comparison of the assumed cumulative afterslip before and after straightening (before and after the correction for viscoelastic relaxation and/or relocking) is shown in Figure S5.

Here we can see the effects of the corrections on the cumulative signal of the data for each model ensemble. Note that for each ensemble we use the model parameters that result in the best fit to the time series after inversion for afterslip and combination of all predictions. For the model of RL + AS, the straightening from RL-only adds a significant southwesterly displacement at all stations in the network meaning that the cumulative displacement assumed to be afterslip is more consistent with the azimuth of plate convergence. For the three-process model, the straightening affects the cumulative signal as a function of distance to the trench. In the near field the displacements are increased in the southwesterly direction. At 70–100 km inland the cumulative displacements are increased in the south direction, and further toward the back arc the cumulative displacements are shortened in an east southeasterly correction. The straightening corrections of the AS + VR ensemble (VR-only straightening) are similar to those of the RL + VR straightening but with slightly less of a southerly magnitude. The differences between straightening corrections and cumulative afterslip signals for the three model ensembles can be seen in Figure S6.

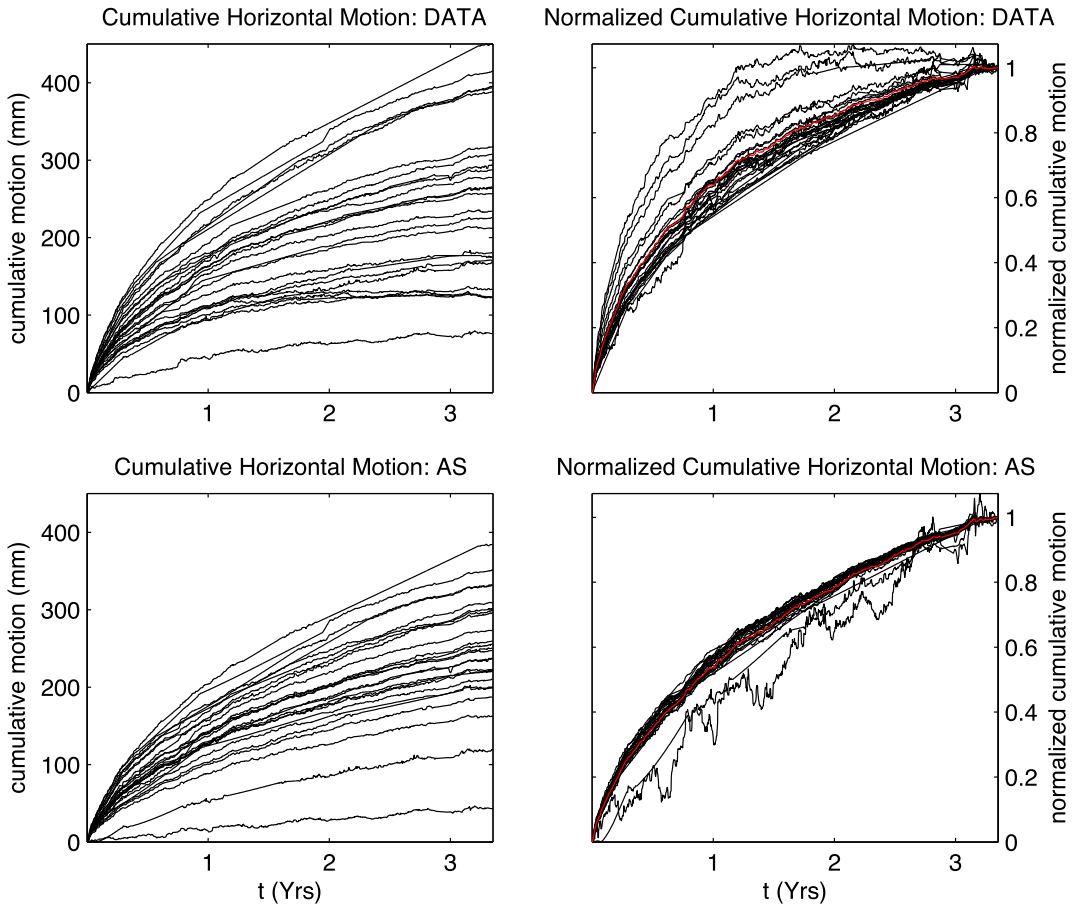

Figure 11. (left column) The cumulative horizontal displacements as a function of time and (right column) the normalized cumulative horizontal displacement time functions, with the mean of the time functions plotted in red. (top row) The data time functions before and after normalization. (bottom row) The remaining afterslip signals following the straightening of the data with the relocking and viscoelastic relaxation (parameters of relocking and viscosities are taken from the model with the best fitting time series following afterslip inversion). The normalized time functions of the straightened (afterslip) signals are much more tightly packed around the mean (red) than in the case of the nonstraightened data, with the exception of a couple of stations.

Figure 7 shows the results of the inversion of the cumulative afterslip signal for each model ensemble and also for the data that have not been straightened. As also shown by *Bedford et al.* [2013], an afterslip model for the data that has not been corrected for other postseismic processes results in a large misfit in the back arc and an unrealistically deep afterslip. All of the correction ensembles (Figures 7b–7d) show a clear improvement in the fit of an afterslip model compared to the nonstraightened data, with the AS + RL + VR and AS + VR ensembles showing roughly the same 67–68% decrease in misfit and the AS + RL ensemble having a 55% decrease in misfit. Misfit is slightly larger in the back arc for the AS + RL ensemble, and the afterslip is of higher magnitude and extends deeper than for the other model ensembles. All of the afterslip models fit poorly the station at 71°W 36°S. Important to note is that these afterslip patterns are not to be interpreted in a mechanical framework of patchwork plate interface frictional heterogeneity since the inclusion of the vertical signal will probably shift the afterslip updip as shown in *Bedford et al.* [2013]. Rather, the exercise of comparing afterslip models is to assess whether the inclusion of the simultaneous nonafterslip postseismic processes leads to an afterslip model with significantly lower misfit and more physically realistic depth extents of the afterslip.

3.5. Comparing Time Series Fits

Figures 8–10 show examples of the misfits at cGPS locations at various distances from the coseismic rupture zone.

The time series discussed in this section use the model parameters that best fit the time series for that particular model ensemble. From these examples and from the rest of the fits (see Figures S9–S33 and Movie S1

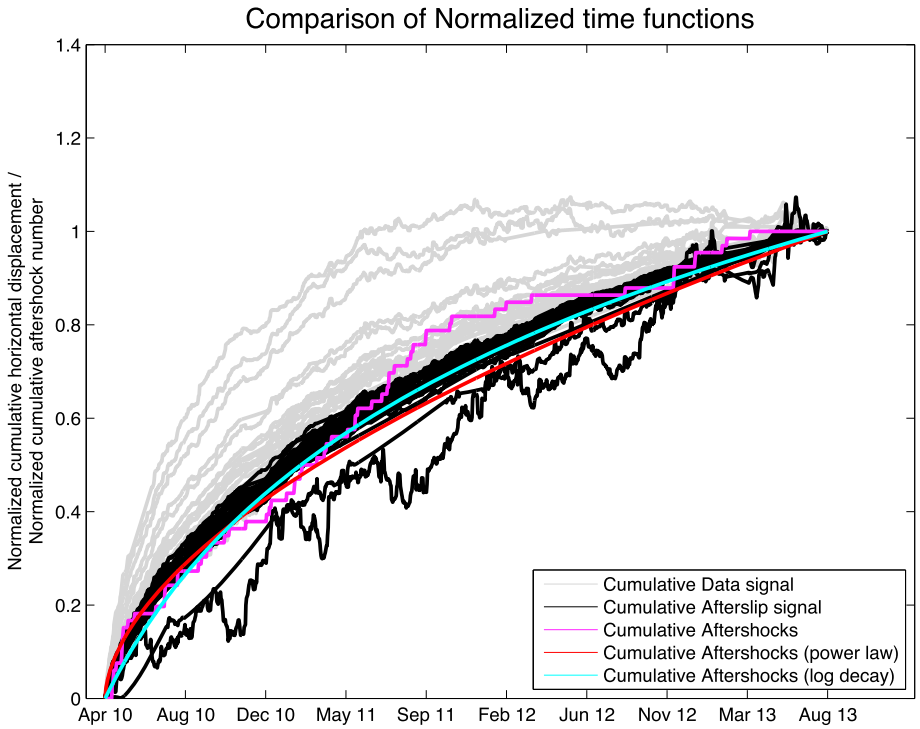

Figure 12. Comparison of the normalized time functions for cumulative aftershock number (events with $M_w > 5$ taken from the IRIS catalogue www.ds.iris.edu) shown by the pink line. Red line shows the power law fit to the pink decay. Normalized time functions of cumulative horizontal motion due to afterslip (straightened data) are shown by the black lines. The normalized time functions of the nonstraightened data are shown in grey. The time functions of cumulative aftershock number and cumulative afterslip are strikingly similar, in agreement with the observations of *Perfettini and Avouac* [2007] and *Lange et al.* [2014].

in the supporting information) we can see that certain ensembles do produce better fits at certain stations, but in general the best fitting ensemble overall is the ensemble of three postseismic processes. For example, at the station CONZ (Figure 8) the AS + RL + VR and the AS + RL ensemble result in the best time series fits, while at the station ANTC (Figure 10), the AS + RL + VR and the AS + VR model ensembles result in the best fits.

3.6. Checking Assumptions of Afterslip Model

We revisit our assumptions from section 2.1 to check if the time functions of the assumed remaining afterslip signal share a similar normalized time function. Figure 11 shows the time functions and their normalized forms for the data before and after straightening for the AS + RL + VR ensemble.

The normalized time functions before the straightening corrections are quite dissimilar, and there is a substantially stronger similarity in the normalized time functions following straightening. There are a couple of stations that deviate with their normalized time functions considerably even after straightening. However, the majority of normalized time functions are grouped tightly and therefore adhere to the expected behavior of the assumed afterslip model (as discussed in section 2.1).

Furthermore, we can compare the normalized afterslip time functions to the normalized cumulative aftershock number. Figure 12 shows that decay in time of the seismicity has a similar normalized time function as the isolated afterslip signal. Such an agreement allows us to state that an independent measure of the normalized decay of megathrust afterslip for the Maule earthquake is, to a good approximation, the decay in the number of cumulative aftershocks.

3.7. Relative Surface Signal Magnitudes of the Simultaneous Postseismic Processes

Figures 13, S7, and S8 show the relative magnitudes and time histories of the simultaneous signals that have been separated by the parameter search. Each model is representative of the model parameters that create

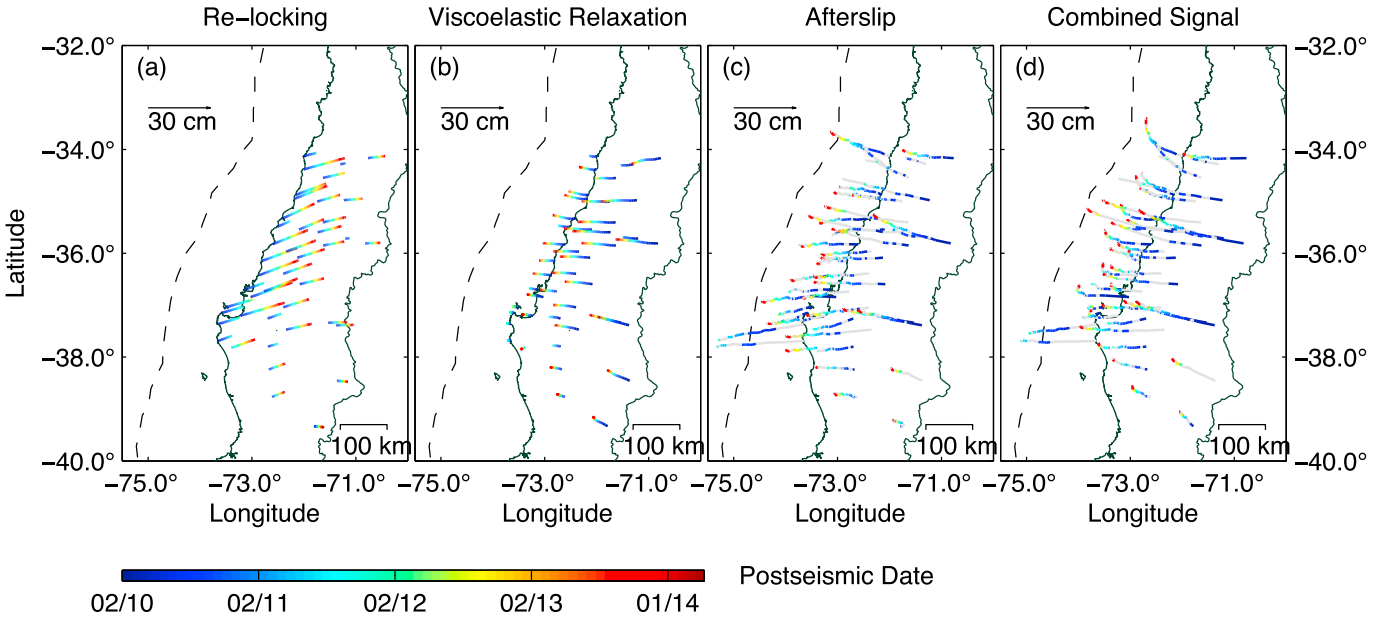

Figure 13. Separation of the relative magnitudes of postseismic processes for best fitting time series model in the ensemble of afterslip, relocking, and viscoelastic relaxation (AS + RL + VR). (a, b) The contribution of relocking and viscoelastic relaxation processes from the optimal model that uses RL + VR straightening. (c) The remaining signal after straightening of the data; this signal can be considered as mainly afterslip. (d) The original data before decomposition into the three processes (Figures 13a–13c). Colors of horizontal deformation pathways in each panel correspond to the time evolution in the color bar. The deformation pathways in Figure 13c are clearly much straighter than those in Figure 13d. Furthermore, the near-field stations after straightening have an increased tendency to move toward the plate convergence azimuth, rather than to the WNW as in the nonstraightened data set. This rotation of azimuth in the straightened data further suggests that the straightened data are the afterslip signal, since these azimuths are reasonable for afterslip opposite to the general direction of plate convergence. A zoom in of this figure at the Arauco Peninsula (−73.5°E, −37.2°N) can be seen in supporting information Figure S9.

the best time series misfits after recombination of all processes in the ensemble. The three-process model (Figure 13) shows the opposing east and west motions of the relocking and viscoelastic relaxation signals. At the coastline, the imbalance of the magnitudes of these signals leads to a slight increase in cumulative displacement magnitude when the relocking and viscoelastic relaxation signals are removed from the data. Compared to the viscoelastic signal, the magnitude of afterslip is generally much larger, with the difference in relative magnitudes decreasing with distance from the rupture zone. The nonuniqueness of the best fitting three-process model ensemble parameters (as seen in Figure 6) can be visualized in supporting information Movie S2: There are of course trade-offs in the amount of landward relocking signal and the strength of the oceanward viscoelastic relaxation and afterslip signals, although for the best 44 solutions, the magnitudes and azimuths of the separated processes are fairly consistent. For the AS + VR model ensemble (Figure S7), the isolated afterslip signal is visibly less straight than in the three-process model. The viscoelastic relaxation model creates landward motion at the coastline, with the hingeline of trenchward displacement at around 70–100 km inland. For the AS + RL model ensemble (Figure S8), the removal of the large relocking signal from the data leaves a cumulative afterslip magnitude that is much larger than for the AS + VR and AS + RL + VR afterslip magnitude.

4. Discussion and Conclusions

4.1. Discussion

The determination of the best combination of simultaneous postseismic processes depends on the expectations of the sensible ranges of model parameters, the expectation of the features of the isolated signals of each process, and the measures of fit for each model ensemble. The three-process ensemble (AS + RL + VR) results in the best fit to the time series, having a 15% lower misfit value than the minimum of the other two ensembles. The realistic spatial distribution of the afterslip model and its good fit to the straightened time series, as well as the azimuthal agreement of the cumulative isolated afterslip signal with the plate convergence direction, strongly support the credibility of the three-process model. Furthermore, the range of oceanic and continental linear Maxwell viscosity combinations in the three-process ensemble are in accordance with contemporary

studies of postseismic relaxation [*Li et al.*, 2015; *Diao et al.*, 2014; *Hu et al.*, 2004; *Bürgmann and Dresen*, 2008]. The AS + VR and AS + RL models both result in a significantly larger misfit to the time series, with the AS + RL model having an unrealistic afterslip distribution consisting of high-magnitude slip at great depths. The isolated afterslip signal of the best fitting AS + VR model exhibits the most veering, and the combinations of mantle viscosities are opposite to what would be expected based on the probable pressure-temperature and compositional conditions either side of the downgoing slab [*Billen and Gurnis*, 2001]. Additionally, these viscosity combinations do not agree with viscosities obtained in other subduction zone postseismic viscoelastic studies [e.g., *Hu and Wang*, 2012]. Considering these features of the model ensembles with respect to the aforementioned criteria, our favored model ensemble is the three-process model.

In addition to other studies suggesting the early onset of relocking in the postseismic phase [*Remy et al.*, 2016; *Azúa et al.*, 2002] this study provides the first explicitly modeled estimates of plate relocking rate following a megathrust subduction event and as such has some important implications for the future of seismic cycle research in similar margins. The rapid relocking time (< 1 year) with respect to the interseismic period means that the current assumption in slip deficit modeling—that the relocking is instantaneous—is reasonable. This assumption of a constant locking-related (secular) velocity is also made when attempting to characterize long-term cGPS time series by means of a trajectory model (e.g., the Extended Trajectory Model of *Bevis and Brown* [2014]). By monitoring seismic velocity recovery in strike-slip faults, *Li et al.* [2006] suggested that gradual strength recovery occurred in the years following the 2004 Parkfield earthquake. Slide-hold tests exploring the strength recovery of the plate interface at realistic stresses and temperatures have shown a rapid strength recovery within minutes at the experimental scale [*Tenthorey et al.*, 2003], with a slowing rate following the initial rapid healing due to mechanisms such as crack closure and solution processes [*Yao et al.*, 2013]. These initially rapid and subsequently decaying rates are supported by our results, suggesting that geodetic observations are appropriate for constraining postseismic strength recovery. An additional independent measure of the coupling state of the plate interface might be inferred from *b* value recovery which has been shown to occur over a just a few years following both the Maule M_w 8.8 (2010) and Tohoku-Oki M_w 9.0 (2011) events [*Tassara et al.*, 2016; *Tormann et al.*, 2015].

The rate of relocking for the best AS + RL + VR parameter combinations can (but not in all solutions) exceed the interseismic rate: Rates from our parameter search indicate that the signal from locking during the postseismic phase could be as much as double the signal from during the interseismic phase. Such an increase in the apparent locking is in accordance with a 50% and 200% increase in locking rates following the earthquakes of Tokachi-Oki (M_w 8.0 2003) and Tohoku-Oki (M_w 9.0 2011), respectively [*Heki and Mitsui*, 2013; *Uchida et al.*, 2016]. From the continued monitoring of this relocking rate we hope to determine the mechanism for such an acceleration, such as the relaxation of a thin low-viscosity layer beneath the slab [*Naif et al.*, 2013; *Heki and Mitsui*, 2013]. Furthermore, the possible relation between an increased slab velocity and the subsequent rupture of the adjacent Illapel segment in 2015 [*Tilmann et al.*, 2016] is a topic for future research.

There is some discord between the Maule near-field observations and the near-field 2011 Japanese Tohoku-Oki M_w 9.0 observations. Following Tohoku-Oki, the landward motion well exceeds the background interseismic rate [*Sun et al.*, 2014] suggesting that another process, other than or in addition to plate interface relocking, is producing such displacements in the near field. One possible explanation is that the offshore GPS stations monitoring the postseismic deformation of Tohoku-Oki are moving in response to a postseismic crustal fault afterslip following the activation of crustal faults during coseismic rupture [*McKenzie and Jackson*, 2012; *Tsuji et al.*, 2011]. The magnitude and pattern of viscoelastic response depends on the magnitude and location of coseismic slip as well as the viscosities and rheologies [*Sun and Wang*, 2015]. In this sense it is conceivable that such a relocking signal as seen for Maule 2010 event may not be so distinguishable in the data for a larger earthquake such as Tohoku-Oki. Furthermore, we recognize that the ongoing efforts to instrument and more frequently measure the submerged surface of the overriding plate will allow a better discrimination between dislocation and viscoelastic relaxation as a cause for curved postseismic motions [*Bürgmann and Chadwell*, 2014].

The separation of the afterslip signal from the other postseismic processes by deducing and removing the veering effect of the simultaneous processes is obviously better constrained by a longer time series. Following a megathrust earthquake, the large aftershocks that can follow can be potentially as destructive as the larger magnitude mainshock, depending on the location, building standards, and regional geology of the nearest human population centers. In terms of a short-term hazard assessment, the slip deficit can be compared

with the after-slipping regions on the plate interface: regions with both a high remaining slip deficit and low afterslip are naturally the zones of highest immediate likelihood of harboring a large aftershock. Future studies should focus on the effects of nonafterslip signal removal on our modeled afterslip: in other words, we should investigate whether or not neglecting nonafterslip processes significantly alters the afterslip model thereby improving the assessment of zones that are at most risk of a high-magnitude aftershock on the plate interface. An example of the ability to identify regions at high risk of large-magnitude plate interface aftershocks with the afterslip model would be the subsequent rupture of the 25 March 2012 Constitución M_w 7.0 aftershock on the plate interface [*Ruiz et al.*, 2013] inside the along-strike rupture extents of the Maule 2010 M_w 8.8. This aftershock, occurring over 2 years after the main shock, occurred in the pocket of low afterslip that had been identified by a model that assumed afterslip as the sole postseismic process contributing to the surface signal [*Bedford et al.*, 2013]. This zone was at a similar depth to adjacent after-slipping zones and aftershock releasing zones and so could be considered as within the seismogenic depth limits. With the basic assumption that all but the highly slipping coseismic zones have the potential to harbor some significant slip deficit, then this zone of low afterslip and relatively low coseismic slip could have been considered to have a high seismic potential. Furthermore, the afterslip model is based on the first year of surface deformation, meaning that with quick enough data retrieval and modeling, this region could have been highlighted as especially prone to a large aftershock in advance of its occurrence. In this case, it seems that the contaminating presence of viscoelastic relaxation and relocking in the postseismic surface signal did not significantly affect the ability to model the heterogeneity in the plate interface postseismic kinematics.

The ability to separate the simultaneous postseismic processes in the case study of Maule 2010 is due to the convenient spread of cGPS locations with respect to the ruptured interface. The magnitude of the veering is larger at stations nearer to the coseismic rupture, and a longer range of distances to the rupture zone makes it easier to distinguish between relocking related veering and viscoelastic relaxation related veering.

In assessing the methods presented in this study we must also address the weaknesses: The separation method of straightening described in this study relies on the assumptions of afterslip behavior as discussed in section 2.1. However, nonstationary migratory behavior of afterslip following a great subduction earthquake has been modeled before (for example, the 2003 Tokachi-Oki M_w 8, Japan [*Ozawa et al.*, 2004]) and therefore the degree of success of the straightening method in separating out simultaneous postseismic processes will depend on the afterslip behavior of the earthquake in question. By the same token, in not accounting for relocking and viscoelastic relaxation in the signal, a modeled afterslip may seem to migrate along the fault interface with time. Therefore, to gauge applicability of the straightening method, we would first recommend repeating the aftershock analysis of section 2.1 (Figure 2) should a suitable aftershock catalogue exist.

The viscoelastic relaxation due to the elastic dislocation of afterslip was not considered in this study: In neglecting this relaxation we must accept that either the isolated viscoelastic relaxation signal (of the coseismic slip) or the isolated relocking signal is contaminated with this additional viscoelastic relaxation. However, due to the magnitude and relatively much slower release of afterslip in comparison to the large and sudden coseismic slip, we do not expect viscoelastic relaxation of the afterslip to be very large in comparison to the coseismic viscoelastic relaxation signal.

An uncertainty that may significantly impact our modeling results is in the chosen dislocation directions for locking and afterslip. To a certain extent we can constrain these directions given the focal mechanics of the foreshock and aftershock catalogues. We are, however, currently unable to estimate how much azimuth should vary as a function of along-strike distance. Additionally, the lack of imposed spatial relations between locked and postseismic slip regions results in some spatial overlap that might seem implausible. We would argue that it is conceivable to have a region on the megathrust that is both postseismically locked and slipping, so long as the slipping occurs discretely rather than as a continuous decay. Furthermore, Laplacian regularization has been applied to both the locking and afterslip models, meaning that any details in the respective distributions are very likely smudged, further promoting spatial overlap. A possible improvement in locating the locking pattern would be to expand the model space by testing a suite of postseismic locking models rather than assuming the persistence of the interseismic locking pattern; however, this would vastly increase the computational expense of the method, especially if we were also allowing a certain freedom in the azimuth of each locked patch. One could also employ an alternative regularization of the afterslip inversion such as sparsity-promoting methods [e.g., *Evans and Meade*, 2012], which would result in tighter regions of modeled afterslip. Any effort to enhance the spatial detail of the dislocation models should carefully be

weighed up against the model resolution afforded by the GPS network and the inherent uncertainties in our knowledge of the acceptable bounds of parameters for the model space. In considering these particular limitations of our case study, the key utility of the straightening method is for providing a first-order estimate of the relative contributions of the three simultaneous postseismic processes in producing the recorded time series and not in producing an upgraded pattern of plate interface kinematics. While we have opted in this study for a simple subduction zone structure with a simple linear Maxwell viscoelastic rheology, the method of straightening would still be just as valid for an alternative structure and rheology [e.g., *Klein et al.*, 2016]. Therefore, this study should be seen primarily as a demonstration of a method to extract simultaneous postseismic processes, with the modeled outputs dependent on the subjective model assumptions.

4.2. Conclusions

In this study we have presented a novel approach for separating the relative contributions of simultaneous postseismic processes and have explored the parameter space for different combinations (ensembles) of these processes. Following the well-founded assumption that a decaying afterslip distribution has a constant relative magnitude, relocking is shown to be the dominant process responsible for the postseismic veering of the cGPS, especially near field to the rupture. Furthermore, the inclusion of relocking along with viscoelastic relaxation and afterslip results in an approximately 15% decrease in the misfitting of the time series. The rapid relocking rates of our favored models are consistent with healing rates that have been shown in lab experimental results and inferred from postseismic seismic velocity observations of strike-slip faults.

The isolation of afterslip with our methodology leaves behind a time function of afterslip that is in good agreement with the time function of cumulative aftershock number. Therefore, the process of afterslip and aftershocks are intrinsically temporally related. The challenge remains in discovering the exact spatiotemporal relationship: namely, the question of whether afterslip is triggering aftershocks through transfer of static stress or if afterslip is triggered by the peturbation to the plate interface from the aftershock series.

Finally, we showed that afterslip distribution is far more realistic (i.e., less deep afterslip needed to fit the data) and produces a much improved data fit when considering viscoelastic relaxation in addition to the afterslip. Afterslip is dominant in the near-field signal in comparison to the viscoelastic relaxation. The credibility of a purely elastic afterslip model is, to a first-order, acceptable and useful for immediate hazard monitoring. However, for this situation one needs to have a cGPS network with near enough station distances to the rupture zone.

An obvious next step for the methods developed in this study would be to fit all three components of the postseismically recorded GPS data so that the optimal model space might be further narrowed down, as well as to test the method at other geodetically well-observed earthquake segments with sufficient availability of cGPS close enough to the subduction trench, for example, with the data of the Illapel 2015 M_w 8.3, Chile, and Iquique 2014 M_w 8.1, Chile.

Acknowledgments

We would like to thank the DFG for granting funds via the PESCADOS project (MO 2310/3-1). We also thank Kosuke Heki and an anonymous reviewer for their helpful peer reviews. For access to the cGPS data presented in this study please contact the CSN, Chile (jcbaez@csn.uchile.cl).

References

Aagaard, B. T., M. G. Knepley, and C. A. Williams (2013), A domain decomposition approach to implementing fault slip in finite-element models of quasi-static and dynamic crustal deformation, *J. Geophys. Res. Solid Earth*, *118*, 3059–3079, doi:10.1002/jgrb.50217.

Altamimi, Z., X. Collilieux, and L. Métivier (2011), Itrf2008: An improved solution of the international terrestrial reference frame, *J. Geod.*, *85*(8), 457–473.

Azúa, B. M., C. DeMets, and T. Masterlark (2002), Strong interseismic coupling, fault afterslip, and viscoelastic flow before and after the Oct. 9, 1995 Colima-Jalisco earthquake: Continuous GPS measurements from Colima, Mexico, *Geophys. Res. Lett.*, *29*(1281), doi:10.1029/2002GL014702.

Bedford, J., et al. (2013), A high-resolution, time-variable afterslip model for the 2010 Maule M_w = 8.8, Chile megathrust earthquake, *Earth Planet. Sci. Lette.*, *383*, 26–36.

Bevis, M., and A. Brown (2014), Trajectory models and reference frames for crustal motion geodesy, *J. Geod.*, *88*(3), 283–311.

Billen, M. I., and M. Gurnis (2001), A low viscosity wedge in subduction zones, *Earth Planet. Sci. Lett.*, *193*(1), 227–236.

Bock, Y., and D. Melgar (2016), Physical applications of GPS geodesy: A review, *Rep. Prog. Phys.*, *79*(10), 106801.

Boehm, J., B. Werl, and H. Schuh (2006), Troposphere mapping functions for GPS and very long baseline interferometry from European Centre for Medium-Range Weather Forecasts operational analysis data, *J. Geophys.Res.*, *111*, B02406, doi:10.1029/2005JB003629.

Bürgmann, R., and D. Chadwell (2014), Seafloor geodesy, *Annu. Rev. Earth Planet. Sci.*, *42*, 509–534.

Bürgmann, R., and G. Dresen (2008), Rheology of the lower crust and upper mantle: Evidence from rock mechanics, geodesy, and field observations, *Annu. Rev. Earth Planet. Sci.*, *36*(1), 531–561.

Bürgmann, R., M. Kogan, V. Levin, C. Scholz, R. King, and G. Steblov (2001), Rapid aseismic moment release following the 5 December, 1997 Kronotsky, Kamchatka, earthquake, *Geophys. Res. Lett.*, *28*(7), 1331–1334.

Dach, R., U. Hugentobler, P. Fridez, and M. Meindl (2007), *Bernese GPS Software Version 5.0*, vol. 640, 114 pp., Astronomical Institute, Univ. of Bern, Bern, Switzerland.

Delouis, B., J.-M. Nocquet, and M. Vallée (2010), Slip distribution of the February 27, 2010 M_w = 8.8 Maule earthquake, central Chile, from static and high-rate gps, insar, and broadband teleseismic data, *Geophys. Res. Lett.*, *37*, L17305, doi:10.1029/2010GL043899.

Diao, F., X. Xiong, R. Wang, Y. Zheng, T. R. Walter, H. Weng, and J. Li (2014), Overlapping post-seismic deformation processes: Afterslip and viscoelastic relaxation following the 2011 M_w 9.0 Tohoku (Japan) earthquake, *Geophys. J. Int.*, *196*(1), 218–229.

Dow, J. M., R. Neilan, and C. Rizos (2009), The international GNSS service in a changing landscape of global navigation satellite systems, *J. Geod.*, *83*(3–4), 191–198.

Evans, E. L., and B. J. Meade (2012), Geodetic imaging of coseismic slip and postseismic afterslip: Sparsity promoting methods applied to the great Tohoku earthquake, *Geophys. Res. Lett.*, *39*, L11314, doi:10.1029/2012GL051990.

Freed, A. M., R. Bürgmann, E. Calais, and J. Freymueller (2006), Stress-dependent power-law flow in the upper mantle following the 2002 Denali, Alaska, earthquake, *Earth Planet. Sci. Lett.*, *252*(3), 481–489.

Hayes, G. P., E. Bergman, K. L. Johnson, H. M. Benz, L. Brown, and A. S. Meltzer (2013), Seismotectonic framework of the 2010 February 27 M_w 8.8 Maule, Chile earthquake sequence, *Geophys. J. Int.*, *195*, 1034–1051, doi:10.1093/gji/ggt238.

Heki, K., and Y. Mitsui (2013), Accelerated Pacific plate subduction following interplate thrust earthquakes at the Japan Trench, *Earth Planet. Sci. Lett.*, *363*, 44–49.

Heki, K., S. Miyazaki, and H. Tsuji (1997), Silent fault slip following an interplate thrust earthquake at the Japan Trench, *Nature*, *386*, 595–598.

Hicks, S. P., A. Rietbrock, C. A. Haberland, I. Ryder, M. Simons, and A. Tassara (2012), The 2010 M_w 8.8 Maule, Chile earthquake: Nucleation and rupture propagation controlled by a subducted topographic high, *Geophys. Res. Lett.*, *39*, L19308, doi:10.1029/2012GL053184.

Hu, Y., and K. Wang (2012), Spherical-earth finite element model of short-term postseismic deformation following the 2004 Sumatra earthquake, *J. Geophys. Res.*, *117*, B05404, doi:10.1029/2012JB009153.

Hu, Y., K. Wang, J. He, J. Klotz, and G. Khazaradze (2004), Three-dimensional viscoelastic finite element model for postseismic deformation of the great 1960 Chile earthquake, *J. Geophys. Res.*, *109*, B12403, doi:10.1029/2004JB003163.

Kanda, R. V., and M. Simons (2010), An elastic plate model for interseismic deformation in subduction zones, *J. Geophys. Res.*, *115*, B03405, doi:10.1029/2009JB006611.

Klein, E., L. Fleitout, C. Vigny, and J. Garaud (2016), Afterslip and viscoelastic relaxation model inferred from the large-scale post-seismic deformation following the 2010 M_w 8.8 Maule earthquake (Chile), *Geophys. J. Int.*, *205*(3), 1455–1472.

Lange, D., J. Bedford, M. Moreno, F. Tilmann, J. Baez, M. Bevis, and F. Krüger (2014), Comparison of postseismic afterslip models with aftershock seismicity for three subduction-zone earthquakes: Nias 2005, Maule 2010 and Tohoku 2011, *Geophys. J. Int.*, *199*(2), 784–799.

Li, S., M. Moreno, J. Bedford, M. Rosenau, and O. Oncken (2015), Revisiting viscoelastic effects on interseismic deformation and locking degree: A case study of the Peru-North Chile subduction zone, *J. Geophys. Res. Solid Earth*, *120*, 4522–4538, doi:10.1002/2015JB011903.

Li, Y.-G., P. Chen, E. S. Cochran, J. E. Vidale, and T. Burdette (2006), Seismic evidence for rock damage and healing on the San Andreas Fault associated with the 2004 M 6.0 Parkfield earthquake, *Bull. Seismol. Soc. Am.*, *96*(4B), S349–S363.

McKenzie, D., and J. Jackson (2012), Tsunami earthquake generation by the release of gravitational potential energy, *Earth Planet. Sci. Lett.*, *345*, 1–8.

Menke, W. (1989), *Geophysical Data Analysis: Discrete Inverse Theory, Int. Geophys. Ser.*, vol. 1, Rev. ed., Academic Press, New York.

Mitrovica, J. X. (1996), Haskell [1935] revisited, *J. Geophys. Res.*, *101*(B1), 555–569.

Moreno, M., M. Rosenau, and O. Oncken (2010), 2010 Maule earthquake slip correlates with pre-seismic locking of Andean subduction zone, *Nature*, *467*(7312), 198–202.

Moreno, M., et al. (2011), Heterogeneous plate locking in the south-central Chile subduction zone: Building up the next great earthquake, *Earth Planet. Sci. Lett.*, *305*(3), 413–424.

Moreno, M., et al. (2012), Toward understanding tectonic control on the M_w 8.8 2010 Maule Chile earthquake, *Earth Planet. Sci. Lett.*, *321*, 152–165.

Naif, S., K. Key, S. Constable, and R. Evans (2013), Melt-rich channel observed at the lithosphere-asthenosphere boundary, *Nature*, *495*(7441), 356–359.

Okada, Y. (1985), Surface deformation due to shear and tensile faults in a half-space, *Bull. Seismol. Soc. Am.*, *75*(4), 1135–1154.

Ozawa, S., M. Kaidzu, M. Murakami, T. Imakiire, and Y. Hatanaka (2004), Coseismic and postseismic crustal deformation after the M_w 8 Tokachi-oki earthquake in Japan, *Earth Planets Space*, *56*(7), 675–680.

Perfettini, H., and J.-P. Avouac (2007), Modeling afterslip and aftershocks following the 1992 Landers earthquake, *J. Geophys. Res.*, *112*, B07409, doi:10.1029/2006JB004399.

Perfettini, H., et al. (2010), Seismic and aseismic slip on the central Peru megathrust, *Nature*, *465*(7294), 78–81.

Radiguet, M., F. Cotton, M. Vergnolle, M. Campillo, B. Valette, V. Kostoglodov, and N. Cotte (2011), Spatial and temporal evolution of a long term slow slip event: The 2006 Guerrero slow slip event, *Geophys. J. Int.*, *184*(2), 816–828.

Remy, D., H. Perfettini, N. Cotte, J. Avouac, M. Chlieh, F. Bondoux, A. Sladen, H. Tavera, and A. Socquet (2016), Postseismic relocking of the subduction megathrust following the 2007 Pisco, Peru, earthquake, *J. Geophys. Res. Solid Earth*, *121*, 3978–3995, doi:10.1002/2015JB012417.

Ruiz, S., et al. (2013), The Constitución earthquake of 25 March 2012: A large aftershock of the Maule earthquake near the bottom of the seismogenic zone, *Earth Planet. Sci. Lett.*, *377*, 347–357.

Savage, J. (1983), A dislocation model of strain accumulation and release at a subduction zone, *J. Geophys. Res.*, *88*(6), 4984–4996.

Sella, G. F., T. H. Dixon, and A. Mao (2002), Revel: A model for recent plate velocities from space geodesy, *J. Geophys. Res.*, *107*(B4), 2081, doi:10.1029/2000JB000033.

Shirzaei, M., R. Bürgmann, N. Uchida, Y. Hu, F. Pollitz, and T. Matsuzawa (2014), Seismic versus aseismic slip: Probing mechanical properties of the northeast Japan subduction zone, *Earth Planet. Sci. Lett.*, *406*, 7–13.

Simons, M., et al. (2011), The 2011 magnitude 9.0 Tohoku-oki earthquake: Mosaicking the megathrust from seconds to centuries, *Science*, *332*(6036), 1421–1425.

Sun, T., and K. Wang (2015), Viscoelastic relaxation following subduction earthquakes and its effects on afterslip determination, *J. Geophys. Res. Solid Earth*, *120*, 1329–1344, doi:10.1002/2014JB011707.

Sun, T., et al. (2014), Prevalence of viscoelastic relaxation after the 2011 Tohoku-oki earthquake, *Nature*, *514*(7520), 84–87.

Tassara, A., and A. Echaurren (2012), Anatomy of the Andean subduction zone: Three-dimensional density model upgraded and compared against global-scale models, *Geophys. J. Int.*, *189*(1), 161–168.

Tassara, A., H. Soto, J. Bedford, M. Moreno, and J. C. Baez (2016), Contrasting amount of fluids along the megathrust ruptured by the 2010 Maule earthquake as revealed by a combined analysis of aftershocks and afterslip, *Tectonophysics*, *671*, 95–109.

Tenthorey, E., S. F. Cox, and H. F. Todd (2003), Evolution of strength recovery and permeability during fluid–rock reaction in experimental fault zones, *Earth Planet. Sci. Lett.*, *206*(1), 161–172.

Tilmann, F., et al. (2016), The 2015 Illapel earthquake, central Chile: A type case for a characteristic earthquake?, *Geophys. Res. Lett.*, *43*, 574–583, doi:10.1002/2015GL066963.

Tormann, T., B. Enescu, J. Woessner, and S. Wiemer (2015), Randomness of megathrust earthquakes implied by rapid stress recovery after the Japan earthquake, *Nat. Geosci.*, *8*(2), 152–158.

Tsuji, T., Y. Ito, M. Kido, Y. Osada, H. Fujimoto, J. Ashi, M. Kinoshita, and T. Matsuoka (2011), Potential tsunamigenic faults of the 2011 off the Pacific coast of Tohoku earthquake, *Earth Planets Space*, *63*(7), 831–834.

Uchida, N., Y. Asano, and A. Hasegawa (2016), Acceleration of regional plate subduction beneath Kanto, Japan, after the 2011 Tohoku-oki earthquake, *Geophys. Res. Lett.*, *43*, 9002–9008, doi:10.1002/2016GL070298.

Vigny, C., et al. (2011), The 2010 M_w 8.8 Maule megathrust earthquake of central Chile, monitored by GPS, *Science*, *332*(6036), 1417–1421.

Wang, K., Y. Hu, and J. He (2012), Deformation cycles of subduction earthquakes in a viscoelastic earth, *Nature*, *484*(7394), 327–332.

Yao, L., T. Shimamoto, S. Ma, R. Han, and K. Mizoguchi (2013), Rapid postseismic strength recovery of Pingxi fault gouge from the Longmenshan fault system: Experiments and implications for the mechanisms of high-velocity weakening of faults, *J. Geophys. Res. Solid Earth*, *118*, 4547–4563, doi:10.1002/jgrb.50308.